Solution of Incompressible Turbulent Flow by a Mesh-Free Method

R. Vertnik[1] **and B. Šarler**[2]

Abstract: The application of the mesh-free Local Radial Basis Function Collocation Method (LRBFCM) in solution of incompressible turbulent flow is explored in this paper. The turbulent flow equations are described by the low - Re number k-ε model with Jones and Launder [Jones and Launder (1971)] closure coefficients. The involved velocity, pressure, turbulent kinetic energy and dissipation fields are represented on overlapping 5-noded sub-domains through collocation by using multiquadrics Radial Basis Functions (RBF). The involved first and second derivatives of the fields are calculated from the respective derivatives of the RBF's. The velocity, turbulent kinetic energy and dissipation equations are solved through explicit time stepping. The pressure-velocity coupling is calculated iteratively, based on the Chorin's fractional step method [Chorin 1967]. The adaptive upwinding technique, proposed by the Lin and Atluri [Lin and Atluri (2000)] is used because of the convection dominated situation. The solution procedure is represented in 2D. Three test cases have been performed: laminar flow in a channel with $Re = 100$, turbulent flow in a channel with $Re = 12300$ and turbulent flow in a channel with 1/6 backward facing step with $Re = 5000$. The solution is compared with the analytical solution in the first case, with the experiment [Laufer (1948)] and commercial code Fluent in the second case, and with the experiment [Jović and Driver (1994)], commercial code Fluent and direct numerical simulation [Le, Moin and Kim (1997)] in the third case. All numerical examples include non-uniform spatial discretisation. A reasonably good agreement between the solutions has been achieved. The advantages of the represented mesh-free approach are its simplicity, accuracy, similar coding in 2D and 3D, and straightforward applicability in non-uniform node arrangements.

Keywords: turbulence, incompressible flow, two-equation turbulence model, k-ε model, radial basis function, multiquadrics, collocation, channel flow, backward

---

[1] Štore-Steel, Techical Development, E-mail: robert.vertnik@p-ng.si
[2] University of Nova Gorica, Laboratory for Multiphase Processes, Slovenia, E-mail: bozidar.sarler@p-ng.si

facing step

1 Introduction

In recent years, a number of mesh-free methods [Atluri and Shen (2002), Atluri (2004), Liu (2003), Liu and Gu (2005)] have been developed to circumvent the problem of polygonisation encountered in the classical numerical methods (finite difference (FDM) and finite volume (FVM) method, finite element method (FEM), boundary domain integral method (BDIM)). In mesh-free methods, approximation is constructed entirely in terms of a set of nodes. There exist a number of meshless methods such as the Element free Galerkin methods, the Meshless local Petrov-Galerkin method, the Point interpolation method, the Point assembly method, the Finite point method, the Finite difference method with arbitrary irregular grids, Smoothed particle hydrodynamics, Reproducing kernel particle method, etc. A class of such methods is based on collocation with radial basis functions [Šarler (2007)]. These functions [Buhmann (2000)] have been first under intensive research in multivariate data and function interpolation [Franke (1982)]. Kansa used them for scattered data approximation [Kansa (1990a)] and than for the solution of partial differential equations [Kansa (1990b)]. The key point of the Radial Basis Function Collocation Method (RBFCM) or Kansa Method (KM) for solving the PDEs is the approximation of the fields on the boundary and in the domain by a set of global approximation functions. The discretization is, respectively, represented only by grid-points (poles of the global approximation functions) in contrast to FEM and BDIM methods where appropriate polygonisation needs to be generated in addition, or FDM, where points are constrained to the coordinate lines. The main advantage of using the RBFCM for solution of partial differential equations is its simplicity, applicability to different PDEs, and effectiveness in dealing with arbitrary dimension and complicated domains. The method recently started to be applied in many scientific and engineering disciplines. It has been first used in the heat transport context by [Zerroukat, Power and Chen (1998)]. The method has been afterwards applied to the classical De Vahl Davis natural convection problem by asymmetric collocation in [Šarler, Perko, Chen and Kuhn (2001)] and additionally by the symmetric and modified collocation in [Šarler (2005)]. The method was used for solution of the Stefan problems [Kovačević, Poredoš and Šarler (2003)], wave equations [Haq, ul-Islam and Ali (2008)] and solid mechanics problems [Mai-Duy, Khennane and Tran-Cong (2007), Le, Mai-Duy, Tran-Cong and Baker (2008)] as well. The method has been formulated instead of deriving the RBF's by integrating the partial derivatives [Mai-Duy, Tran-Cong (2003)] and applied to transient problems [Mai-Cao and Tran-Cong (2005)] fluid flow [Mai-Duy, Mai-Cao, Tran-Cong (2007)] and moving boundaries [Mai-Cao and Tran-Cong (2008)]. Several

other special developments of the method have been deduced such as the improved treatment of the Neumann boundary conditions [Libre, Emdadi, Kansa, Rahimian and Shekarchi (2008)].

The main disadvantage of the mentioned method represent the related full matrices that are very sensitive to the choice of the free parameter in RBFs and are difficult to solve for problems of the order of 10^3 unknowns or larger. The solution of related problem has been attempted by domain decomposition [Mai-Duy and Tran-Cong (2002)], multi-grid approach and compactly supported RBFs [Chen, Ganesh, Golberg and Cheng (2002)] which all represent a substantial complication of the original simple method. The radial basis functions have been first put into context of porous media flow by [Šarler, Gobin, Goyeau, Perko and Power (2000)] where the natural convection problem in Darcy porous media, and later Darcy-Brinkman porous media [Šarler, Perko, Gobin, Goyeau and Power (2004)] have been solved by the dual reciprocity boundary element method (DRBEM). This method belongs to the semi-mesh-free methods, because the domain fields are approximated by the global interpolation with the RBFs and the boundary fields by the boundary elements (polygons). The truly mesh-free RBFCM has been for the first time used for solution of Darcy porous media in [Šarler, Perko and Chen (2004)]. A substantial breakthrough in the development of the RBFCM was its local formulation, LRBFCM. This formulation was first developed for diffusion problems [Šarler and Vertnik (2006)], than to convection-diffusion problems with phase-change [Vertnik and Šarler (2006)], to industrial application of direct chill casting of aluminum alloys [Vertnik, Zalonik and Šarler (2006)], continuous casting of steel [Vertnik and Šarler (2008)], to solid-solid phase transformations [Kovačević and Šarler (2005)] and to solution of Navier Stokes equations [Divo and Kassab (2007), Kosec and Šarler (2008a)] and porous media flow [Kosec and Šarler (2008b)]. A similar, local quadrature based RBF approach, was developed by [Shu, Ding and Yeo (2005)]. The main issue of the local version of the RBFCM is the collocation on a sub-set of, in general, overlapping sub-domains, which drastically reduces the collocation matrix size on the expense of solving many small matrices instead of a large one. Since the method does not experience significant accuracy drawback in comparison with the global version, it represents a practical choice also for solving very large problems. The main goal of this work is to upgrade the LRBFCM for solving complex engineering turbulence models, which is by the best knowledge of the present authors, a pioneering effort in the development of the meshless methods. In the last century, a lot of research has been devoted towards understanding of the turbulent flows. In spite of those attempts, a general physical theory still does not exist. Numerically, those flows could be very well predicted by the direct numerical simulation (DNS) of the Navier-Stokes equations. Unfortunately, in the

DNS very fine spatial discretization has to be used in order to model and track all eddies of the flow, especially the smallest ones. The applicability of the DNS is currently limited to very simple geometries and for turbulent flows with moderate Reynolds (Re) numbers [Le, Moin and Kim (1997)]. Other turbulent models are mainly derived through the time-averaging of the Navier-Stokes (N-S) equations. Due to the nonlinearity of the time-averaged N-S equations, a closure problem arises (more unknowns than equations), which puts these family of models into the category of semi-empirical ones. Various models were proposed [Wilcox (1993)], which are rather old, but still in use nowadays. Probably the most known and representative is the family of two-equation k-ε models, which are further divided into two groups, standard and low-Re models. The standard k-ε models use the wall-functions, while the low-Re models use special closure coefficients to correctly predict the turbulent boundary layers. Better predictions are obtained with the low-Re models, but a very fine disretization near the walls is required. In this work, the low-Re k-ε model is used with the closure coefficients proposed by [Jones and Launder (1971)].

The present paper is structured in the following way. The governing equations of the incompressible turbulent flow are presented first. The general initial and boundary conditions for the velocity, pressure, turbulent kinetic energy k and dissipation ε are described. The explicit solution procedure of the governing equations is proposed, where the fractional step method [Chorin (1967)] is used to couple the velocity and pressure fields. The discretization is made by the LRBFCM by using multiquadrics on five-noded sub-domains. Due to the convection-dominated problems, the adaptive upwind technique (AUT) is introduced. At the end, the proposed numerical method is assessed through three numerical examples: laminar two-dimensional channel flow, turbulent two-dimensional channel flow, and turbulent flow over a backward-facing step. The results are compared with the analytical solution, experiments, DNS and the most recent version 6.3 of the commercial software Fluent.

2   Governing equations

Consider a connected fixed domain Ω with boundary Γ filled with a fluid that exhibits incompressible turbulent flow. The flow is described (in a two-dimensional Cartesian coordinate system with base vectors $\mathbf{i}_\varsigma$; $\varsigma = x, y$ and coordinates p_ς; $\varsigma = x, y$, i.e. position of point $\mathbf{p}$ is determined as $\mathbf{p} = \mathbf{i}_\varsigma p_\varsigma$; $\varsigma = x, y$) by the following time-averaged Reynolds equations for mass conservation, and momentum conservation in x and y directions

$$\frac{\partial v_x}{\partial p_x} + \frac{\partial v_y}{\partial p_y} = 0, \tag{1}$$

$$\frac{\partial v_x}{\partial t} + v_x \frac{\partial v_x}{\partial p_x} + v_y \frac{\partial v_x}{\partial p_y} =$$

$$- \frac{1}{\rho} \frac{\partial p}{\partial p_x} + \frac{\partial}{\partial p_x} (v + v_t) \left(2 \frac{\partial v_x}{\partial p_x} \right) + \frac{\partial}{\partial p_y} (v + v_t) \left(\frac{\partial v_x}{\partial p_y} + \frac{\partial v_y}{\partial p_x} \right), \quad (2)$$

$$\frac{\partial v_y}{\partial t} + v_x \frac{\partial v_y}{\partial p_x} + v_y \frac{\partial v_y}{\partial p_y} =$$

$$- \frac{1}{\rho} \frac{\partial p}{\partial p_y} + \frac{\partial}{\partial p_y} (v + v_t) \left(2 \frac{\partial v_y}{\partial p_y} \right) + \frac{\partial}{\partial y} (v + v_t) \left(\frac{\partial v_y}{\partial p_x} + \frac{\partial v_x}{\partial p_y} \right), \quad (3)$$

with v_x and v_y standing for the time averaged velocity components in x- and y-direction, respectively, and p, t, ρ, v and v_t standing for pressure, time, density, molecular kinematic viscosity and turbulent kinematic viscosity, respectively. Molecular kinematic viscosity is defined as

$$v = \frac{\mu}{\rho} \quad (4)$$

where μ is molecular dynamic viscosity. Turbulent kinematic viscosity is defined as

$$v_t = c_\mu f_\mu \frac{k^2}{\varepsilon}. \quad (5)$$

In Eq. (5) c_μ and f_μ are closure coefficients of the turbulence model, and k and ε are the turbulent kinetic energy and dissipation, calculated by the following transport equations

$$\frac{\partial k}{\partial t} + v_x \frac{\partial k}{\partial p_x} + v_y \frac{\partial k}{\partial p_y} =$$

$$\frac{\partial}{\partial p_x} \left(v + \frac{v_t}{\sigma_k} \right) \frac{\partial k}{\partial p_x} + \frac{\partial}{\partial p_y} \left(v + \frac{v_t}{\sigma_k} \right) \frac{\partial k}{\partial p_y} + P_k - \varepsilon + D, \quad (6)$$

$$\frac{\partial \varepsilon}{\partial t} + v_x \frac{\partial \varepsilon}{\partial p_x} + v_y \frac{\partial \varepsilon}{\partial p_y} =$$

$$\frac{\partial}{\partial p_x} \left(v + \frac{v_t}{\sigma_\varepsilon} \right) \frac{\partial \varepsilon}{\partial p_x} + \frac{\partial}{\partial p_y} \left(v + \frac{v_t}{\sigma_\varepsilon} \right) \frac{\partial \varepsilon}{\partial p_y} + (c_{1\varepsilon} f_1 - c_{2\varepsilon} f_2 \varepsilon) \frac{\varepsilon}{k} + E, \quad (7)$$

where P_k, D and E are the shear production of turbulent kinetic energy, source term in k equation and source term in ε equation, respectively. They are given by

$$P_k = v_t \left(2 \left(\frac{\partial v_x}{\partial p_x} \right)^2 + 2 \left(\frac{\partial v_y}{\partial p_y} \right)^2 + \left(\frac{\partial v_x}{\partial p_y} + \frac{\partial v_y}{\partial p_x} \right)^2 \right), \quad (8)$$

$$D = -2v \left[\left(\frac{\partial \sqrt{k}}{\partial p_x} \right)^2 + \left(\frac{\partial \sqrt{k}}{\partial p_y} \right)^2 \right], \tag{9}$$

$$E = 2vv_t \left[\left(\frac{\partial^2 v_x}{\partial p_y^2} \right)^2 + \left(\frac{\partial^2 v_y}{\partial p_x^2} \right)^2 \right], \tag{10}$$

In Eqs. (5) and (7), the closure coefficients c_μ, f_μ, $c_{1\varepsilon}$, f_1, $c_{2\varepsilon}$, f_2, σ_k and σ_ε of the low-Reynolds turbulent model [Jones and Launder (1971)] are defined as

$$c_\mu = 0.09, \tag{11}$$

$$f_\mu = \exp \left(\frac{-2.5}{1 + Re_t/50} \right), \tag{12}$$

$$c_{1\varepsilon} = 1.45, \tag{13}$$

$$f_1 = 1.0, \tag{14}$$

$$c_{2\varepsilon} = 2.00, \tag{15}$$

$$f_2 = 1 - 0.3 \exp \left(-Re_t^2 \right), \tag{16}$$

$$\sigma_k = 1.0, \tag{17}$$

$$\sigma_\varepsilon = 1.3. \tag{18}$$

The turbulent Reynolds number Re_t (used in Eqs. (12) and (16)) is defined as

$$Re_t = \frac{k^2}{v\varepsilon} \tag{19}$$

In order to determine the turbulent flow, the system of Eqs. (1), (2), (3), (6) and (7) has to be solved.

3   Solution procedure

We seek the solution of the x and y velocity components, pressure field, k and ε fields at time $t + t_0$ by assuming known fields v_x, v_y, p, k and ε at time t_0 and known boundary conditions. The coupled set of mass conservation Eq. (1) and momentum conservation Eqs. (2), (3) are solved by the fractional step method [Chorin (1967)], where the continuity of the mass Eq. (1) is considered by constructing and solving the pressure Poisson equation. At every time step, the following explicit numerical algorithm is used

Step 1: The intermediate velocity components v_x^* and v_y^* are calculated first, without considering the pressure gradient

$$
v_x^* = v_{x0} + \frac{\rho}{\Delta t}
$$
$$
\left[-v_x \frac{\partial v_x}{\partial p_x} - v_y \frac{\partial v_x}{\partial p_y} + \frac{\partial}{\partial p_x} (v + v_t) \left(2 \frac{\partial v_x}{\partial p_x} \right) + \frac{\partial}{\partial y} (v + v_t) \left(\frac{\partial v_x}{\partial p_y} + \frac{\partial v_y}{\partial p_x} \right) \right]_0, \tag{20}
$$

$$
v_y^* = v_{y0} + \frac{\rho}{\Delta t}
$$
$$
\left[-v_x \frac{\partial v_y}{\partial p_x} - v_y \frac{\partial v_y}{\partial p_y} + \frac{\partial}{\partial p_y} (v + v_t) \left(2 \frac{\partial v_y}{\partial p_y} \right) + \frac{\partial}{\partial y} (v + v_t) \left(\frac{\partial v_y}{\partial p_x} + \frac{\partial v_x}{\partial p_y} \right) \right]_0, \tag{21}
$$

where index 0 represents initial conditions at time $t = t_0$.

Step 2: The pressure Poisson equation is solved

$$
\nabla^2 p = \frac{\rho}{\Delta t} \left(\frac{\partial v_x^*}{\partial p_x} + \frac{\partial v_y^*}{\partial p_y} \right) \tag{22}
$$

The pressure equation can be solved by converting it into a diffusion equation [Divo and Kassab (2007)] or by solving the sparse matrix [Lee, Liu and Fan (2003)]. An additional possibility represents the use of the local pressure correction [Kosec and Šarler (2008)] which seems to be most efficient. However the last correction has not been yet successfully tested for inflow and outflow situations. In this work, the approach [by Lee, Liu and Fan (2003)] is used, where the solution of the sparse matrix is solved by the direct method. In case of the fixed node arrangement, the left-hand side of the sparse matrix can be L-U decomposed before the first time step. This numerical approach significantly improves the performance, since only

the back substitution is used to solve the pressure field at each time step. The boundary conditions for the pressure equation are explicitly given in the Section 5.

Step 3: The intermediate velocity components are corrected through the calculated pressure gradient at time $t = t_0 + \Delta t$

$$v_x = v_x^* - \frac{\Delta t}{\rho} \frac{\partial p}{\partial p_x}, \tag{23}$$

$$v_y = v_y^* - \frac{\Delta t}{\rho} \frac{\partial p}{\partial p_y}, \tag{24}$$

Step 4: After the solution of the velocity field, given in steps 1÷3, the transport Eqs. (6) and (7) of the turbulence model at time $t = t_0 + \Delta t$ are solved

$$k = k_0 + \Delta t \left[-v_x \frac{\partial k}{\partial p_x} - v_y \frac{\partial k}{\partial p_y} + \frac{\partial}{\partial p_x} \left(v + \frac{v_t}{\sigma_k} \right) \frac{\partial k}{\partial p_x} + \right.$$
$$\left. \frac{\partial}{\partial p_y} \left(v + \frac{v_t}{\sigma_k} \right) \frac{\partial k}{\partial p_y} + P_k - \varepsilon + D \right]_0, \tag{25}$$

$$\varepsilon = \varepsilon_0 + \Delta t \left[-v_x \frac{\partial \varepsilon}{\partial p_x} - v_y \frac{\partial \varepsilon}{\partial p_y} + \frac{\partial}{\partial p_x} \left(v + \frac{v_t}{\sigma_\varepsilon} \right) \frac{\partial \varepsilon}{\partial p_x} + \right.$$
$$\left. \frac{\partial}{\partial p_y} \left(v + \frac{v_t}{\sigma_\varepsilon} \right) \frac{\partial \varepsilon}{\partial p_y} + (c_{1\varepsilon} f_1 - c_{2\varepsilon} f_2 \varepsilon) \frac{\varepsilon}{k} + E \right]_{t=t_0}. \tag{26}$$

Step 5: The turbulent viscosity is updated from Eq. (5), and the solution is ready for the next time step.

The block diagram of the described algorithm is schematically represented in Figure 3.1.

4   Initial conditions

It is well known that all involved four transport Eqs. (20), (21), (25) and (26) are strongly coupled. So it is very important how we choose the initial conditions for each transport variable. The initial conditions for velocity components are obtained by solving the potential field

$$\nabla^2 \phi = 0 \tag{27}$$

where ϕ stands for the velocity potential. Laplace Eq. (27) is solved by the same approach as pressure Eq. (22). The following boundary conditions are used.
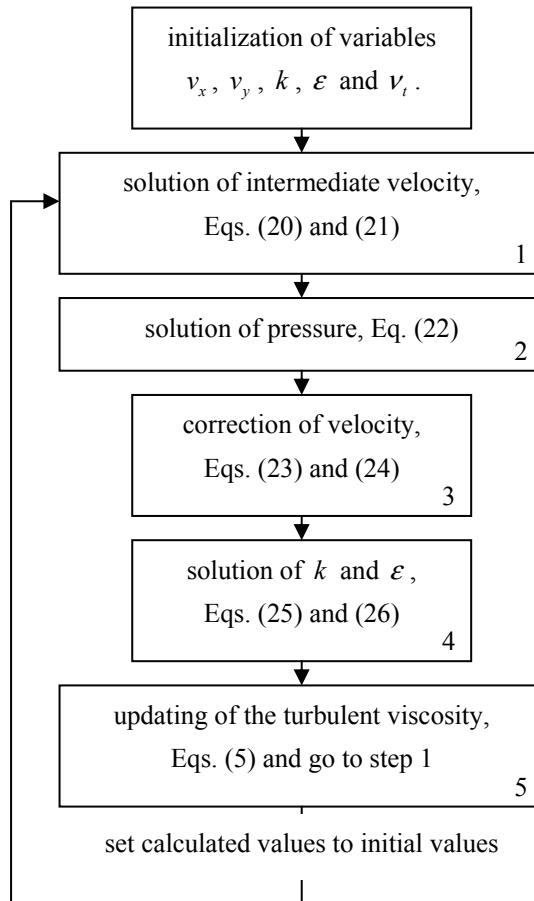
Figure 3.1: Block diagram of the numerical algorithm.

- At the inlet boundaries and solid walls, the Neumann boundary conditions for velocity potential are prescribed

$$\frac{\partial \phi}{\partial p_x} n_x + \frac{\partial \phi}{\partial p_y} n_y = -\left(v_{0x} n_x + v_{0y} n_y\right) \tag{28}$$

- At the outlet boundaries, the Dirichlet boundary conditions for velocity potential are set to

$$\phi = 0 \tag{29}$$

After solving the potential flow field, the velocity field in the domain is obtained by the following relations

$$v_{0x} = \frac{\partial \phi}{\partial p_x}, \quad v_{0y} = \frac{\partial \phi}{\partial p_y} \tag{30}$$

This procedure guarantees the solenoidality of the initial velocity field.

In order to prescribe the proper initial conditions for k and ε, two different techniques might be employed:

- Use of the uniform profile for both k and ε. A few thousand time steps must usually be performed with smaller time step to achieve the consistency between the velocity, pressure, turbulent energy and dissipation equation. When the large mismatch of the transport variables at initial times is reduced, larger time steps can be used.

- Use of the assumption of turbulent equilibrium [Yoder and Georgiadis (1999)], where the production of turbulent kinetic energy equals the rate of dissipation. In order to use this technique, another turbulence model, usually algebraic model, is first run to get initial values of the turbulent viscosity.

In this work, the turbulence transport variables are initialized by the first approach.

5   Boundary conditions

Four different types of boundaries are considered in the present paper: inlet, outlet, symmetry, and wall. The following boundary conditions are used at these boundaries:

- At the inlet boundary, the Dirichlet boundary conditions for velocity components, k and ε are prescribed.

- At the outlet boundary, the Neumann boundary conditions for velocity components, k and ε are prescribed and set to zero.

- At the symmetry line, the same Neumann boundary conditions as for the outlet boundary are used, except for the velocity component, perpendicular to the symmetry line, where the Dirichlet boundary conditions are prescribed and set to zero.

- At the wall, the Dirichlet no-slip boundary conditions are set, which implies that the velocity components, k and ε are all set to zero.

Boundary conditions for pressure Eq. (22) at inlet, symmetry, and wall boundaries are of the Neumann type, i.e.,

$$\frac{\partial p}{\partial p_x} n_x + \frac{\partial p}{\partial p_y} n_y = \frac{1}{\Delta t} \left(\varphi_x n_x + \varphi_y n_y \right) \tag{31}$$

where the n_x and n_y are the components of the normal vector in x and y directions. φ_x and φ_y have the following form

$$\varphi_x = v_x^* - v_{x,0}^w \tag{32}$$

$$\varphi_y = v_y^* - v_{y,0}^w \tag{33}$$

where v_x^* and v_y^* are intermediate velocities, solved by the Eqs. (20) and (21) at the wall. In Eqs. (32) and (33), the $v_{x,0}^w$ and $v_{y,0}^w$ represents the wall velocities at t_0. At the outlet boundary, the Dirichlet boundary conditions for pressure are used and set to zero.

6 Radial basis function collocation method

The representation of function Φ over a set of l (in general) non-equally spaced $_lN$ nodes $_l\mathbf{p}_n$; $n = 1, 2, \ldots, {}_lN$ is made in the following way

$$\Phi(\mathbf{p}) \approx \sum_{k=1}^{_lK} {}_l\psi_k(\mathbf{p}) {}_l\alpha_k \tag{34}$$

$_l\psi_k$ stands for the shape functions, $_l\alpha_k$ for the coefficients of the shape functions, and $_lK$ represents the number of the shape functions. The left lower index on entries of Eq. (34) represents the domain of influence $_l\omega$ on which the coefficients $_l\alpha_k$ are determined. The domains of influence $_l\omega$ can in general be contiguous (overlapping) or non-contiguous (non-overlapping). Each of the domains of influence $_l\omega$ includes $_lN$ grid-points of which $_lN_\Omega$ are in the domain and $_lN_\Gamma$ are on the boundary. Typical domains of influence are shown in Figure 6.1.

The coefficients can be calculated from the nodal values in the domain of influence in two distinct ways. The first way is collocation (interpolation) and the second way is approximation by the least squares method. Only the more simple collocation version for calculation of the coefficients is considered in this paper. Let us assume the known function values $_l\Phi_n$ in the nodes $_l\mathbf{p}_n$ of the domains of influence $_l\omega$. The collocation implies

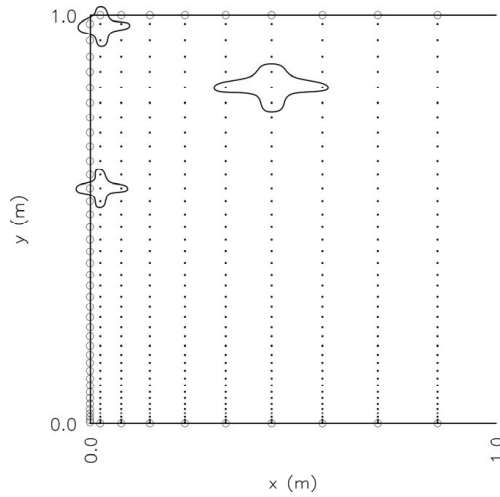$$\Phi({}_l\mathbf{p}_n) = \sum_{k=1}^{_lN} {}_l\psi_k({}_l\mathbf{p}_n) {}_l\alpha_k \tag{35}$$

Figure 6.1: Typical corner, boundary, and interior 5-noded domains of influence.

For the coefficients to be computable, the number of the shape functions has to match the number of the collocation points $_lK = {}_lN$, and the collocation matrix has to be non-singular. The system of Eqs. (35) can be written in a matrix-vector notation

$$_l\psi_l\alpha = {}_l\Phi; \quad {}_l\psi_{kn} = {}_l\psi_k\left({}_l\mathbf{p}_n\right); \quad {}_l\Phi_n = \Phi\left({}_l\mathbf{p}_n\right) \tag{36}$$

The coefficients $_l\alpha$ can be computed by inverting the system (36)

$$_l\alpha = {}_l\psi^{-1}{}_l\Phi \tag{37}$$

By taking into account the expressions for the calculation of the coefficients $_l\alpha$, the collocation representation of function $\Phi(\mathbf{p})$ on domain of influence $_lw$ can be expressed as

$$\Phi(\mathbf{p}) \approx \sum_{k=1}^{_lN} {}_l\psi_k(\mathbf{p}) \sum_{n=1}^{_lN} {}_l\psi_{kn}^{-1}{}_l\Phi_n \tag{38}$$

The first partial spatial derivatives of $\Phi(\mathbf{p})$ in the domain of influence $_lw$ can be expressed as

$$\frac{\partial}{\partial p_\varsigma}\Phi(\mathbf{p}) \approx \sum_{k=1}^{_lN} \frac{\partial}{\partial p_\varsigma}{}_l\psi_k(\mathbf{p}) \sum_{n=1}^{_lN} {}_l\psi_{kn}^{-1}{}_l\Phi_n; \quad \varsigma = x, y \tag{39}$$

The second partial spatial derivatives of $\Phi(\mathbf{p})$ in the domain of influence $_l w$ can be expressed as

$$\frac{\partial^2}{\partial p_\varsigma p_\xi}\Phi(\mathbf{p}) \approx \sum_{k=1}^{lN} \frac{\partial^2}{\partial p_\varsigma p_\xi}\, _l\psi_k(\mathbf{p}) \sum_{n=1}^{lN}\, _l\psi_{\mathrm{kn}}^{-1}\, _l\Phi_n;$$

$$\varsigma,\xi = x,y \tag{40}$$

The radial basis functions, such as multiquadrics, can be used for the shape function

$$_l\psi_k(\mathbf{p}) = \left[_lr_k^2 + c^2\right]^{1/2} \tag{41}$$

where c represents the shape parameter and $_lr_0$ the radial distance between two points in the sub-domain. The $_lr_k$ is scaled by the maximum distance between sub-domain points in x and y direction

$$_lr_k^2 = \left(\frac{p_x - p_{kx}}{p_{x\,\max}}\right)^2 + \left(\frac{p_y - p_{ky}}{p_{y\,\max}}\right)^2 \tag{42}$$

where $p_{x\,\max}$ is the maximum distance between any of the sub-domain points in the x direction and $p_{y\,\max}$ is the maximum distance between any of the sub-domain points in the y direction.

The shape parameter c is fixed for all sub-domains, and set to 32 [Šarler and Vertnik (2006), Vertnik and Šarler (2006)] in all numerical examples of the present paper. The accuracy of the results increases with increased value of the shape parameter, however the condition number of the collocation matrix worsens. The chosen value 32 represents a reasonable balance between both trends. All sub-domains are chosen to contain five nodes as depicted in Figure 6.1.

7 Adaptive upwind technique

The turbulent flows belong to the convection dominated problems. If the spatial discretization is not sufficiently fine, the solution becomes instable or oscillatory. Without any additional numerical efforts, the LRBFCM on uniform node spacing, gives similar oscillations as the central FDM discretization on uniform node spacing, i.e. the solution starts to oscillate when the Péclet number (based on the node spacing) is greater than two. To stabilize the numerical solution, the adaptive upwind technique [Lin and Atluri (2000)] is used, where the adaptive upwind displacement is constructed based on the local Péclet number. This technique was already found to be very useful in the numerical modeling of the heat transfer in the continuous casting of steel [Vertnik, Šarler, Bulinski and Manojlović (2007)].

In the adaptive upwind support technique, the expansion coefficients are first calculated by the LRBFCM. The derivatives of the convection terms are then calculated in the point $p_{\varsigma\Delta}$, shifted by the central offset distance Δp_ς in the opposite direction of the current velocity, see Figure 7.1. The position of the shifted point $p_{\Delta\varsigma}$ is defined as

$$p_{\Delta\varsigma} = p_\varsigma - \Delta p_\varsigma; \quad \varsigma = x, y \tag{43}$$

The central offset distance is calculated by

$$\Delta p_\varsigma = \text{sign}(v_x)\, \delta \frac{h}{2}; \quad \varsigma = x, y \tag{44}$$

where δ is the upwind function and h is the maximal distance between the central point and the neighboring point in the opposite direction of the velocity, as shown in Figure 7.1. The upwind function, represented in Figure 7.2, is defined as

$$\delta = \coth\left|Pe_\varsigma\right| - \frac{1}{\left|Pe_\varsigma\right|}; \quad \varsigma = x, y \tag{45}$$

and the local Péclet number as

$$Pe = \frac{v_x\left(p_x^+ - p_x^-\right)}{v + v_t} \tag{46}$$
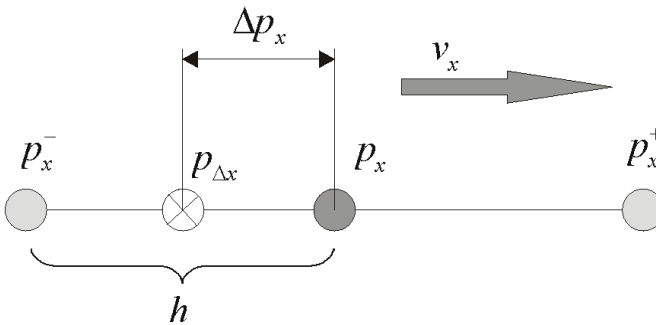

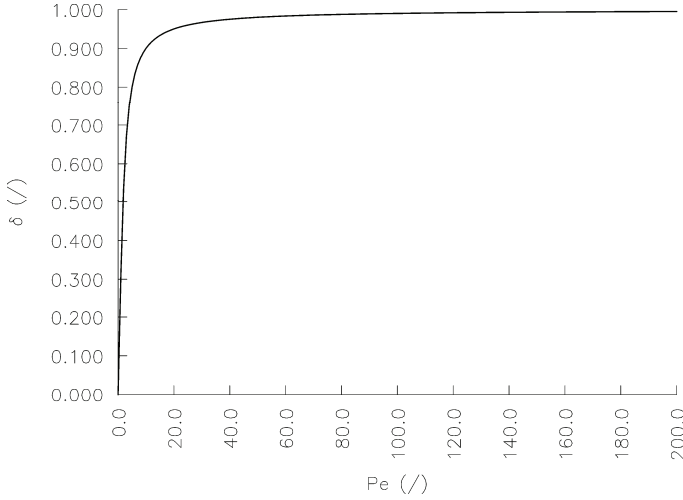
Figure 7.1: Adaptive upwind support in x-direction.

Figure 7.2: Upwind function.

8   Numerical examples

Three numerical examples are represented in the present work. The first example shows the ability of the developed numerical method to solve the laminar incompressible flows. The second example employs the same geometry as the first example, but with included turbulence. The last example represents a well known test for various turbulence models: a 1/6 backward-facing step channel flow. In all three examples, the time step Δt is equal to 10^{-3} s and kept constant through the entire simulation.

8.1   *Laminar 2D channel flow*

The physical domain is a 2D channel with length L and height D. In our computations, only one half of a channel with height $H = D/2$ is considered, as shown in Figure 8.1. The length of the channel is large enough to achieve the fully developed flow at the channel outlet. The density and the inlet velocity are both equal to unity, while the kinematic viscosity v is calculated from the Reynolds number

$$Re = \frac{v_x \cdot H}{v}. \tag{47}$$

The computation was performed with $Re_H = 100$, where $H = 1.0\,m$. The irregular node arrangement with 4137 nodes (41x101 nodes without 4 corner nodes) was
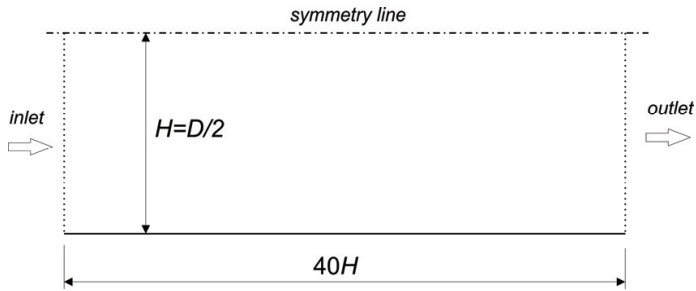
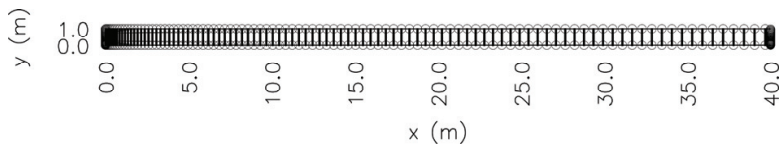Figure 8.1: Geometry of the 2D channel flow.

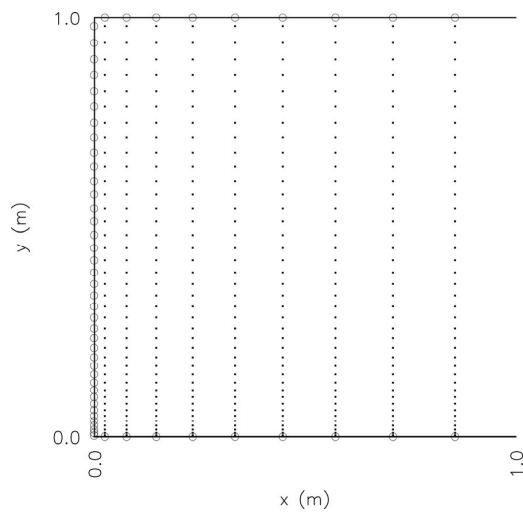Figure 8.2: The node arrangement with 4137 nodes.

Figure 8.3: The detailed view of the node arrangement. Points - interior nodes, circles - boundary nodes.
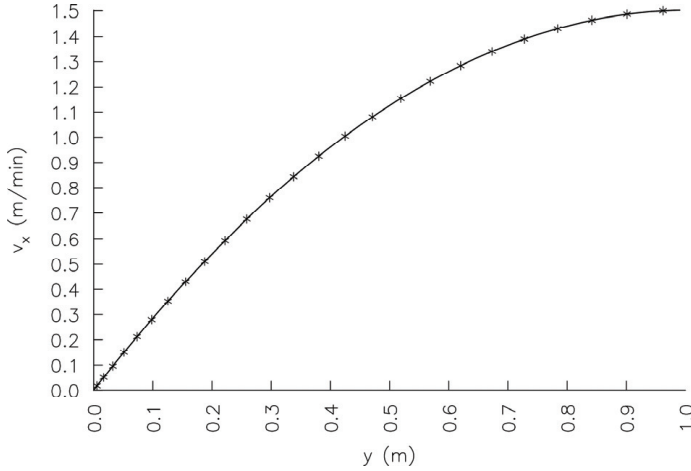
Figure 8.4: Horizontal velocity v_x at the channel outlet. Solid line - present method, symbols * – analytical solution.

used. The arrangement is shown in Figure 8.2 and Figure 8.3. The calculated velocity v_x at the channel outlet was compared with the following analytical solution

$$v_{x,ana}(y) = \frac{3}{2} v_{x,inlet} \left(1 - \left(\frac{2y}{D} \right)^2 \right) \tag{48}$$

The comparison is shown in Figure 8.4. An excellent agreement is observed between both solutions.

8.2 Turbulent 2D channel flow

The same geometry and node arrangement as used in the previous example is used in this example as well. Additionally, the turbulence model is included. The computation was performed with Reynolds number $Re_H = 12300$. The turbulent quantities at the inlet are defined by the following relations

$$k_{in} = \frac{3}{2} (i_0 \cdot v_{x,in})^2, \quad \varepsilon_0 = C_\mu^{3/4} \frac{k_{in}^{3/2}}{0.07H} \tag{49}$$

where i_0 is the turbulent intensity, set to 4 %. The results are compared with the experiments [Laufer (1948)] and with the results obtained by the commercial software Fluent. In Fluent, the calculation was performed by the uniform mesh with 64000 quadrilateral cells, and the k-ε turbulent model with standard wall functions

was set. The results are shown in Figure 8.5, where the normalized velocity v_x at the channel outlet is shown. Numerical values of both numerical methods, evaluated at the experiment positions, are tabulated in Table 1.
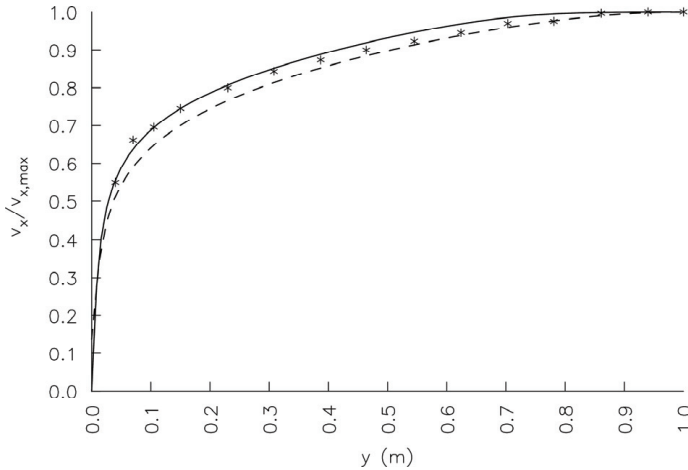

Figure 8.5: Normalized velocity v_x at the channel outlet. Solid line – present method, dashed line – Fluent, and symbols * – measurements.

8.3 Backward facing step

The geometry of the physical domain is taken from the experiment by [Jović and Driver (1994)] and shown in Figure 8.6. The experiment is characterized by the step height $H = 1.0$, the channel length after the step $L = 30H$ and by the Reynolds number $Re_H = 5000$, which determines the inlet conditions at the step. The computational domain considers only the physical domain after the step. In the experiment, the fully developed flow was achieved at the $3H$ distance before the step with the Reynolds number based on the momentum thickness $Re_\theta = 610$. The Re_θ is defined as

$$Re_\theta = \frac{\theta \cdot v_{x\Gamma}}{\nu} \qquad (50)$$

where θ is the momentum thickness and $v_{x\Gamma}$ is the inlet velocity of the air, measured in the channel far away upstream of the step. Both quantities are taken directly from the experiment and have values $\theta = 0.12\ cm$ and $v_{x\Gamma} = 7.72\ m/s$.

In order to achieve the same inlet conditions at the step as in the experiment, the fully developed flow was first calculated with the 2D channel numerical simulation,

Table 1: Tabulated normalized velocity v_x at the channel outlet

y(m)	experiment[*]	present method	Fluent[♣]
0.040	0.5498	0.5541	0.5107
0.070	0.6615	0.6367	0.5897
0.105	0.6956	0.6943	0.6477
0.150	0.7449	0.7448	0.7002
0.230	0.7998	0.8067	0.7660
0.308	0.8434	0.8515	0.8134
0.387	0.8737	0.8884	0.8524
0.464	0.9000	0.9190	0.8845
0.545	0.9229	0.9468	0.9136
0.624	0.9456	0.9691	0.9383
0.703	0.9703	0.9858	0.9596
0.781	0.9759	0.9951	0.9770
0.861	0.9968	0.9988	0.9905
0.949	1.0000	0.9998	0.9982
1.000	1.0000	1.0000	1.0000

* [Laufer (1948)]
♣ Fluent, version 6.3

as described in the second example of this paper. The calculated profiles of v_x, v_y, k, ε and v_t were considered as the inlet conditions of the channel at the step. Other boundary conditions are the same as in the second example. The node arrangement was generated with adaptation near the walls, see Figure 8.7. The detailed view of the node arrangement near the walls is shown in Figure 8.8.

The results are compared with the measurements [Jović and Driver (1994)] (JD), with the results obtained by the direct numerical simulation (DNS) of turbulent flow [Le, Moin and Kim (1997)], and with the results obtained by the commercial software (FLUENT).

In Fluent, the calculation was performed by the uniform mesh with 288000 cells (mesh 1200×240 cells) and with the same turbulent model as in the first example. With this very fine mesh, a reasonable mesh-independence of the results has been achieved. The same boundary conditions and material properties were set as in the LRBFCM calculations.

The calculated velocity v_x at different x/H positions is compared with the results obtained by other methods. For better insight of the obtained results, the velocity v_x profile at each x/H position is plotted into its own figure: at $x/H = 4$ in Figure
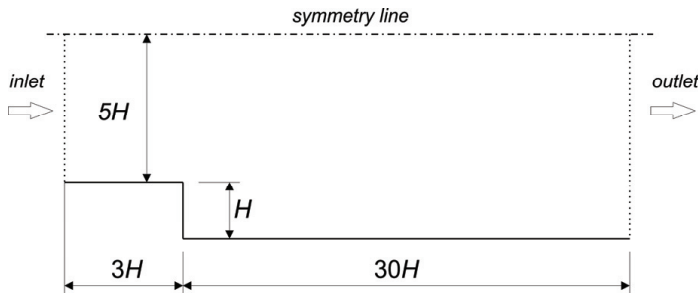
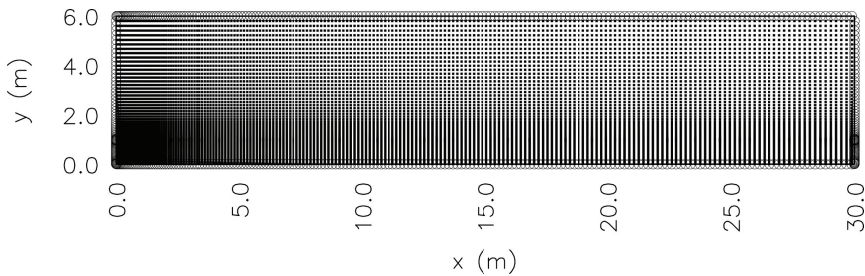Figure 8.6: The physical domain of the backward-facing step.

Figure 8.7: Node arrangement with 14267 nodes for geometry in Figure 8.6 (rotated for 90 deg.).

8.10, at $x/H = 6$ in Figure 8.11, at $x/H = 10$ in Figure 8.12, at $x/H = 15$ in Figure 8.13 and at $x/H = 19$ in Figure 8.14. Below each figure, the numerical and experimental velocity values v_x are also tabulated in Table 2, 3, 4, 5 and 6. The small differences between all methods and experiment are more clearly visible from the tabulated values. There are several reasons, why those differences are expected. The prevailing one is in using different turbulence models, where each model has its own advantages and weaknesses. DNS should probably be the most accurate, since the Navier-Stokes equations are directly solved.

The important quantity in the backward-facing step simulations is the reattachment length, were the fluid separates. The reattachment position can be obtained based on the horizontal velocity v_x at the first inner point, closest to the bottom wall. The separation is at the position were the velocity v_x is equal to zero. The separation position at $x/H = 6.28$ is obtained with the present method. The related reattachment positions obtained by experiment and other numerical methods are represented in Table 7.
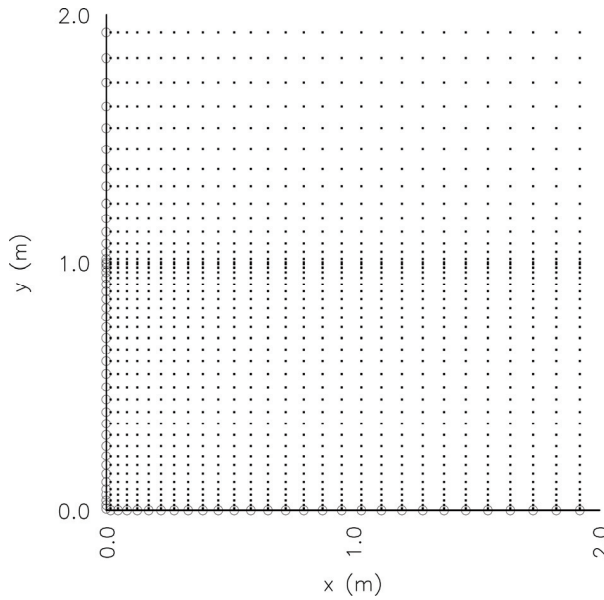
Figure 8.8: The detailed view of the node arrangement. Points - interior nodes, circles - boundary nodes.
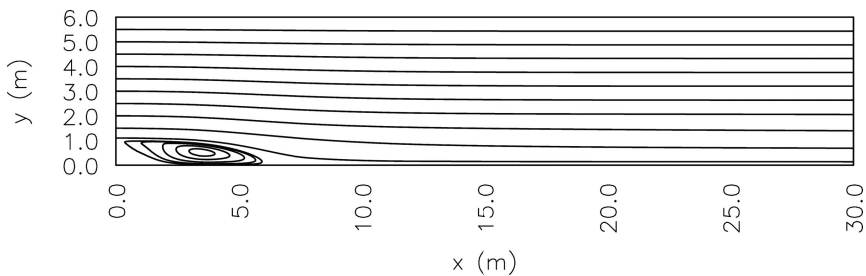
Figure 8.9: Streamlines calculated with the LRBFCM (rotated for 90 deg.).

8.4 Global continuity calculation

The global continuity of the RBF collocation method was checked for internal flows in [Kosec and Šarler (2008a)]. In this paper, the global continuity is checked for discussed three types of channel flows by calculating the mean velocity across the inlet

$$\bar{V}_{in} = \frac{1}{\Delta y_{in}} \int\limits_{y_{in}} v_x(y)\,dy + \frac{1}{\Delta y_{in}} \int\limits_{y_{in}} v_y(y)\,dy, \tag{51}$$

Figure 8.10: The normalized velocity v_x at $x/H = 4$. Solid line – LRBFCM, dashed line – FLUENT, Δ – DNS and * – JD.

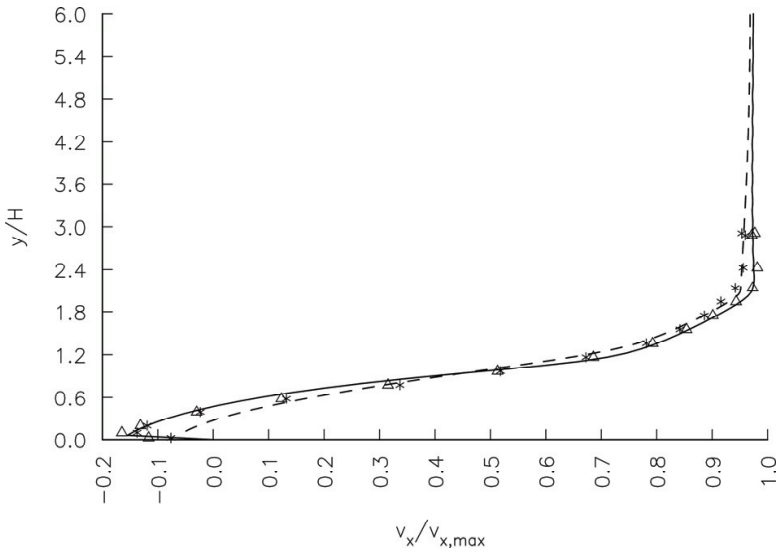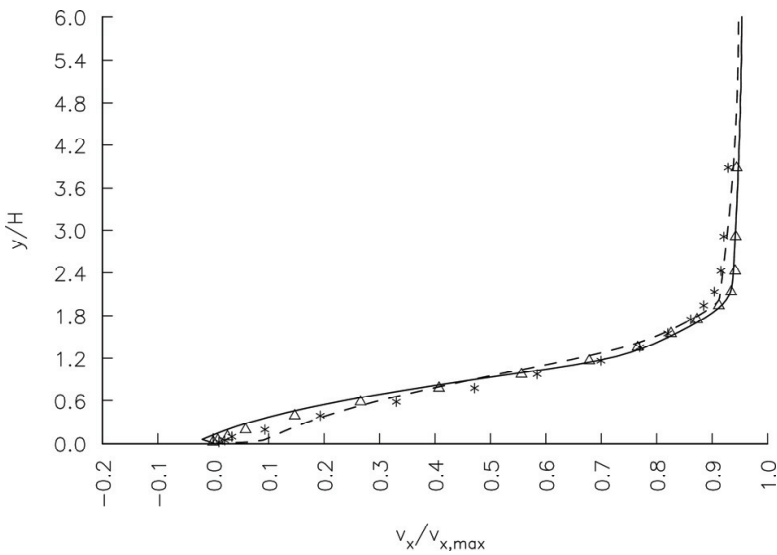Figure 8.11: he normalized velocity v_x at $x/H = 6$. Solid line – LRBFCM, dashed line – FLUENT, Δ - DNS and * - JD.

Table 2: Normalized velocity v_x at $x/H = 4$.

	experiment*	present method	DNS$^\Delta$	FLUENT$^\clubsuit$
0.025	-0.0764	-0.0634	-0.1164	-0.0621
0.097	-0.1373	-0.1463	-0.1647	-0.0546
0.194	-0.1192	-0.1193	-0.1314	-0.0272
0.388	-0.0233	-0.0419	-0.0299	0.0532
0.582	0.1321	0.0731	0.1230	0.1655
0.776	0.3368	0.2448	0.3153	0.3083
0.970	0.5181	0.4894	0.5129	0.4759
1.164	0.6723	0.7108	0.6857	0.6450
1.358	0.7811	0.8000	0.7928	0.7644
1.552	0.8420	0.8584	0.8537	0.8319
1.746	0.8860	0.9081	0.9012	0.8845
1.940	0.9158	0.9511	0.9433	0.9300
2.134	0.9417	0.9733	0.9730	0.9516
2.425	0.9559	0.9747	0.9816	0.9535
2.910	0.9534	0.9728	0.9770	0.9571
3.880	0.9598	0.9729	0.9716	0.9569

* [Jović and Driver (1994)]
Δ [Le, Moin and Kim (1997)]
♣ Fluent, version 6.3

and the outler surfaces

$$\bar{V}_{out} = \frac{1}{\Delta y_{out}} \int\limits_{y_{out}} v_x(y)\,dy + \frac{1}{\Delta y_{out}} \int\limits_{y_{out}} v_y(y)\,dy. \tag{52}$$

Ideally, the scaled difference η

$$\eta = \frac{\bar{V}_{in} - \bar{V}_{out}}{\bar{V}_{in}} \cdot 100\%. \tag{53}$$

between both average velocities should be zero to maintain the mass continuity. In the laminar flow case, depicted in Figure 8.4: $\eta = 0.56\%$, in the turbulent flow case, depicted in Figure 8.5: $\eta = 1.50\%$, and in the turbulent flow case, depicted in Figure 8.9: $\eta = 1.36\%$, respectively.

Table 3: Normalized velocity v_x at $x/H = 6$.

	experiment*	present method	DNS$^\Delta$	FVM♣
0.025	0.0104	-0.0058	-0.0002	0.0668
0.049	0.0207	-0.0151	0.0083	0.0891
0.097	0.0337	-0.0083	0.0257	0.1052
0.194	0.0933	0.0246	0.0583	0.1347
0.388	0.1930	0.1097	0.1471	0.2037
0.582	0.3303	0.2248	0.2657	0.2915
0.776	0.4715	0.3700	0.4073	0.3970
0.970	0.5842	0.5384	0.5560	0.5154
1.164	0.6995	0.6931	0.6783	0.6362
1.358	0.7694	0.7788	0.7656	0.7395
1.552	0.8199	0.8346	0.8258	0.8106
1.746	0.8614	0.8814	0.8727	0.8622
1.940	0.8847	0.9164	0.9122	0.9025
2.134	0.9041	0.9329	0.9343	0.9148
2.425	0.9158	0.9383	0.9416	0.9195
2.910	0.9210	0.9415	0.9426	0.9268

Figure 8.12: The normalized velocity v_x at $x/H = 10$. Solid line – LRBFCM, dashed line – FLUENT, Δ - DNS and * - JD.

Table 4: Normalized velocity v_x at $x/H = 10$.

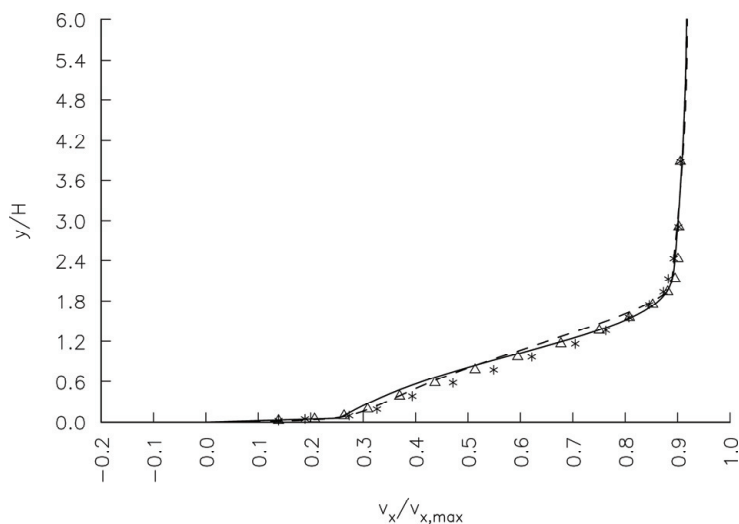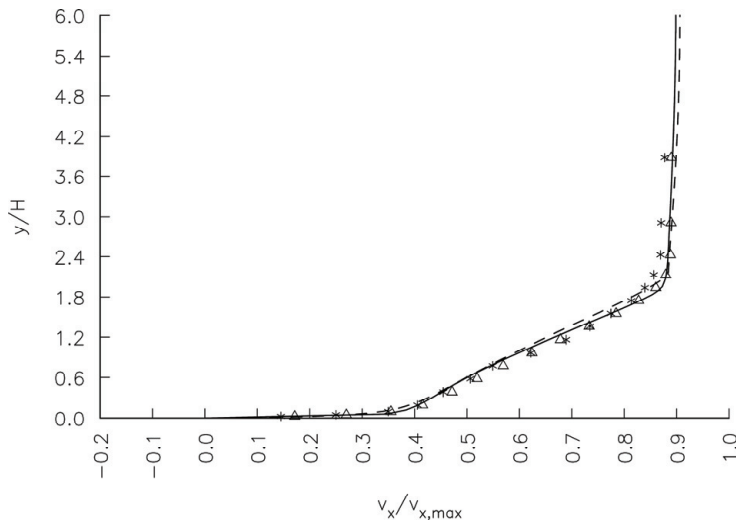|	experiment*	present method	DNS$^\Delta$	FVM♣
0.025	0.1386	0.1035	0.1386	0.1737
0.049	0.1891	0.2028	0.2073	0.2285
0.097	0.2733	0.2625	0.2636	0.2706
0.194	0.3264	0.2864	0.3086	0.3102
0.388	0.3938	0.3400	0.3697	0.3677
0.582	0.4715	0.4064	0.4370	0.4262
0.776	0.5492	0.4850	0.5135	0.4911
0.970	0.6218	0.5728	05949	0.5620
1.164	0.7047	0.6642	0.6774	0.6371
1.358	0.7629	0.7483	0.7505	0.7124
1.552	0.8070	0.8119	0.8079	0.7822
1.746	0.8458	0.8546	0.8524	0.8398
1.940	0.8730	0.8792	0.8811	0.8797
2.134	0.8821	0.8898	0.8951	0.8893
2.425	0.8925	0.8952	0.9006	0.8928
2.910	0.9015	0.9000	0.9024	0.8989

Figure 8.13: The normalized velocity v_x at $x/H = 15$. Solid line – LRBFCM, dashed line – FLUENT, Δ - DNS and * - JD.

Table 5: The normalized velocity v_x at $x/H = 15$.

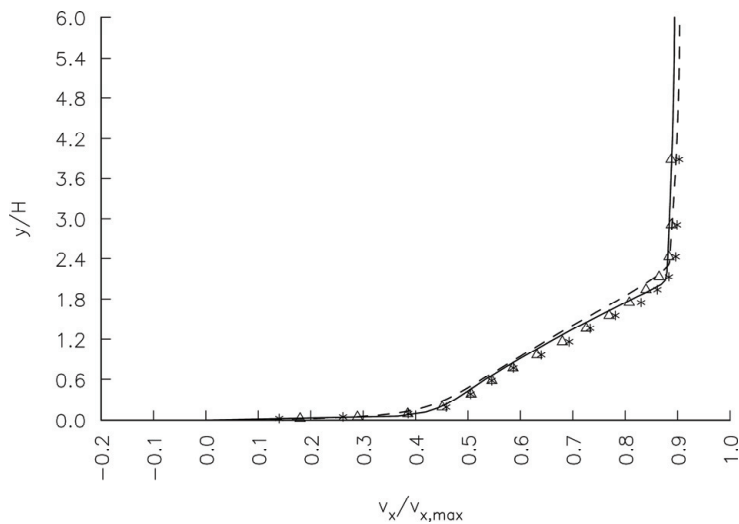|	experiment[*]	present method	DNS[Δ]	FVM[♣]
0.025	0.1451	0.1416	0.1714	0.2011
0.049	0.2500	0.2775	0.2698	0.2721
0.097	0.3497	0.3687	0.3549	0.3361
0.194	0.4054	0.4062	0.4154	0.3895
0.388	0.4547	0.4513	0.4717	0.4473
0.582	0.5065	0.4959	0.5192	0.4944
0.776	0.5492	0.5449	0.5692	0.5415
0.970	0.6218	0.5985	0.6239	0.5906
1.164	0.6891	0.6559	0.6782	0.6420
1.358	0.7344	0.7154	0.7332	0.6951
1.552	0.7746	0.7745	0.7845	0.7485
1.746	0.8135	0.8299	0.8275	0.8000
1.940	0.8394	0.8703	0.8602	0.8467
2.134	0.8562	0.8800	0.8792	0.8815
2.425	0.8692	0.8837	0.8882	0.8862
2.910	0.8705	0.8867	0.8894	0.8908

Figure 8.14: The normalized velocity v_x at $x/H = 19$. Solid line – LRBFCM, dashed line – FLUENT, Δ - DNS and * - JD.

Table 6: The normalized velocity v_x at $x/H = 19$.

	experiment*	present method	DNS$^\Delta$	FVM$^\clubsuit$
0.025	0.1399	0.1495	0.1798	0.2068
0.049	0.2616	0.2931	0.2892	0.2823
0.097	0.3860	0.3975	0.3852	0.3551
0.194	0.4585	0.4458	0.4509	0.4174
0.388	0.5052	0.4910	0.5061	0.4785
0.582	0.5453	0.5296	0.5457	0.5225
0.776	0.5868	0.5693	0.5859	0.5634
0.970	0.6399	0.6115	0.6316	0.6045
1.164	0.6930	0.6562	0.6801	0.6466
1.358	0.7332	0.7031	0.7256	0.6898
1.552	0.7811	0.7513	0.7693	0.7337
1.746	0.8303	0.8000	0.8078	0.7775
1.940	0.8614	0.8498	0.8397	0.8196
2.134	0.8834	0.8778	0.8646	0.8575
2.425	0.8964	0.8814	0.8836	0.8853
2.910	0.8990	0.8840	0.8879	0.8894

Table 7: Reattachment length.

	reattachment length - x/H
experiment*	6.00±0.15
present method	6.28
DNS$^\Delta$	6.28
FVM$^\clubsuit$	5.50

9 Conclusions

This paper probably for the first time represents the solution of the incompressible turbulent flow by a meshless method. Various turbulent models and numerical methods were used in the past to solve such kind of problems. In the present method, we used the low-Re k-ε model with the closure coefficients proposed by Jones and Launder (1971). Other low-Re turbulence models can be used in the present method [Wilcox (1993)], but the user should be careful about the boundary conditions for k and ε of each model. The numerical solution is based on the local collocation with the radial basis functions for spatial disretization and first order (backward Euler) explicit method for time discretization. Due to its locality and

explicit time stepping, the method is very appropriate for parallelization. The partial differential equations are solved in their strong formulation, hence no integration are needed. The transition from two-dimensional to three-dimensional cases is quite straightforward. Three examples were focused to test the accuracy and applicability of the proposed method. In the first example, the laminar two-dimensional channel flow was simulated, where we show the capability of the fractional step method to solve the incompressible flows. The sparse solver was used to solve the pressure Poison's equation. The results were compared with the analytical solution and experiment. Turbulent flow in a two-dimensional channel and turbulent flow over a backward-facing step, were chosen in the next two examples, based on availability of the experimental and numerical tests. In the future, various casting problems [Vertnik and Šarler (2009)] will be simulated, where the heat and species transfer with solidification is involved in addition to the turbulent flow. With this, the new LRBFCM will most probably achieve reasonable maturity.

References

Atluri, S.N.; Shen, S. (2002): *The Meshless Method*, Tech Science Press, Encino.

Atluri, S.N. (2004): *The Meshless Method (MLPG) for Domain and BIE Discretization*, Tech Science Press, Forsyth.

Buhmann, M.D. (2000): *Radial Basis Functions*, Cambridge University Press, Cambridge.

Chen, C. S.; Ganesh, M.; Golberg, M. A.; Cheng, A. H. D. (2002): Multilevel compact radial basis functions based computational scheme for some elliptic problems. *Computers and Mathmathics with Applications*, vol. 43, pp. 359-378.

Chorin, A. J. (1967): A numerical method for solving incompressible viscous flow problems. *Journal of Computational Physics*, vol. 2, pp. 12-26.

Divo, E.; Kassab, A. J. (2007): An efficient localized RBF meshless method for fluid flow and conjugate heat transfer. *ASME Journal of Heat Transfer*, vol. 129, pp. 124-136.

Franke, J. (1982): Scattered data interpolation: tests of some methods. *Mathematics of Computation*, vol. 48, pp. 181-200.

Gu, Y.T.; Liu, G.R. (2005): Meshless technique for convection dominated problems. *Computational Mechanics*, vol. 38, pp. 171-182.

Haq, S.; ul-Islam, S.; Arshed, A. (2008): A numerical meshfree technique for the solution of the MEW equation, *CMES: Computer Modeling in Engineering & Sciences*, vol. 38, pp. 1-24.

Jones, W.P.; Launder, B.E. (1971): The prediction of laminarization with a two-equation model of turbulence. *International Journal of Heat and Mass Transfer*, vol. 15, pp. 301–314.

Jović, S.; Driver, D.M. (1994): Bacward-Facing Step Measurements at Low Reynolds Number, $Re_H = 5000$. *NASA Technical Memorandum 108807*.

Kansa, E. J. (1990b): Multiquadrics – a scattered data approximation scheme with application to computational fluid dynamics, part II. *Computers and Mathematics with Applications*, vol. 19, pp. 147-161.

Kansa, E. J. (1990a): Multiquadrics – a scattered data approximation scheme with application to computational fluid dynamics, part I. *Computers and Mathematics with Applications*, vol. 19, pp. 127-145.

Kosec, G.; Šarler, B.: (2008a): Solution of thermo-fluid problems by collocation with local pressure correction, *International Journal of Numerical Methods in Heat and Fluid Flow*, vol. 18. pp. 868-882.

Kosec, G.; Šarler, B. (2008b): Local radial basis function collocation method for Darcy flow, *CMES: Computer Modeling in Engineering & Sciences*, vol.25, pp.197-207.

Kovačević, I.; Poredo?, A.; Šarler, B. (2003). Solving the Stefan problem with the radial basis function collocation method. *Numer. heat transf., B Fundam.*, vol. 44, pp. 1-24.

Kovačević, I.; Šarler, B. (2005): Solution of a phase-field model for dissolution of primary particles in binary aluminum alloys by an r-adaptive mesh-free method. *Materials Science and Engineering A*, vol. 413–414, pp. 423–428.

Laufer, J. (1948): Investigation of turbulent flow in a two-dimensional channel. *PHD Thesis*, California Institute of Technology, Pasadena, California.

Le, H.; Moin, P.; Kim, J. (1997): Direct numerical simulation of turbulent flow over a backward-facing step. *Journal of Fluid Mechanics*, vol. 330, pp. 349–374.

Le, P.; Mai-Duy, N; Tran-Cong, T.; Baker, G. (2008): A meshless modeling of dynamic strain localization in quasi-brittle materials using radial basic function networks, *CMES: Computer Modeling in Engineering & Sciences*, vol. 25, pp. 43-66.

Lee, C.K.; Liu, X.; Fan, S.C. (2003): Local multiquadric approximation for solv-

ing boundary value problems. *Computational Mechanics*, vol. 30, pp. 396–409.

Libre, N.A.; Emdadi, A.; Kansa, E.J.; Rahimian, M.; Shekarchi, M. (2008): A stabilised RBF collocation scheme for Neumann type boundary conditions. *CMES: Computer Modeling in Engineering & Sciences*, vol. 24, pp. 61–80.

Lin, H., Atluri, S.N.. (2000) Meshless local Petrov-Galerkin (MLPG) method for convection-diffusion *CMES: Computer Modeling in Engineering & Sciences*, vol.1. 45-60.

Lin, H, Atluri, S.N. (2001) The Meshless Local Petrov-Galerkin (MLPG) method for solving incompressible Navier-Stokes equations, *CMES: Computer Modeling in Engineering & Sciences*, vol. 2, pp. 117-142.

Liu, G.R. (2003): *Mesh Free Methods*, CRC Press, Boca Raton.

Liu, G.R.; Gu, Y.T. (2005): *An Introduction to Meshfree Methods and Their Programming*, Springer, Dordrecht.

Mai-Cao, L.; Tran-Cong, T. (2005): A meshless IRBFN-based method for transient problems, *CMES: Computer Modeling in Engineering & Sciences*, vol. 7, pp. 149-171.

Mai-Cao, L.; Tran-Cong, T. (2008): A meshless approach to capturing moving interfaces in passive transport problems, *CMES: Computer Modeling in Engineering & Sciences*, vol. 31, pp. 157-188.

Mai-Duy, N.; Tran-Cong, T. (2003): Indirect RBFN method with thin plate splines for numerical solution of differential equations, *CMES: Computer Modeling in Engineering & Sciences*, vol. 4, pp. 85-102.

Mai-Duy, N.; Khennane, A.; Tran-Cong, T. (2007): Computation of laminated composite plates using integrated radial basis function networks, *CMC: Computers, Materials, & Continua*, vol. 5, pp. 63-78.

Mai-Duy, N.; Mai-Cao, L.; Tran-Cong, T. (2007): Computation of transient viscous flows using indirect radial basic function networks, *CMES: Computer Modeling in Engineering & Sciences*, vol. 18, pp. 59-77.

Perko, J.; Šarler, B. (2007): Weigh function shape parameter optimization in meshless methods for non-uniform grids. *CMES: Computer Modelling in Engineering and Sciences*, vol. 19, pp. 55-68.

Shu, C.; Ding, H.; Yeo, K. S. (2005): Computation of incompressible Navier-Stokes equations by local RBF-based differential quadrature method. *CMES*, vol. 7, pp. 195-205.

Šarler, B. (2005): A radial basis function collocation approach in computational fluid dynamics. *CMES: Computer Modelling in Engineering & Sciences*, vol. 7, pp. 185-193.

Šarler, B. (2007): From global to local radial basis function collocation method for transport phenomena, *Advances in Meshfree Techniques*, Springer, Berlin, pp. 257-282.

Šarler, B.; Perko, J.; Chen, C. S.; Kuhn, G. (2001): A meshless approach to natural convection, *International Conference on Computational Engineering and Sciences, CD proceedings.*

Šarler, B.; Vertnik, R. (2006): Meshfree explicit local radial basis function collocation method for diffusion problems. *Computers and Mathematics with Applications*, vol. 51, pp. 1269-1282.

Vertnik, R.; Šarler, B. (2006): Meshless local radial basis function collocation method for convective-diffusive solid-liquid phase change problems. *International Journal of Numerical Methods for Heat and Fluid Flow*, vol. 16, pp. 617-640.

Vertnik, R.; Zalonik, M.; Šarler, B. (2006): Solution of transient direct-chill aluminium billet casting problem with simultaneous material and Interphase moving boundaries by a meshless method. *Engineering Analysis with Boundary Elements*, vol. 30, pp. 847-855.

Vertnik, R.; Šarler, B.; Bulinski, Z.; Manojlović, G. (2007): Solution of transient temperature field in continuous casting of steel by a meshless method, *Second International Conference of Simulation and Modelling of Metallurgical Processes in Steelmaking*, Graz, Austria, September 2007, ASMET.

Vertnik, R.; Šarler, B.; (2009): Solution of continuous casting of steel by a meshless method, *Cast Metals Research*, 2009, in print.

Wilcox, D.C. (1993): *Turbulence modeling for CFD*, DCW Industries, California.

Yoder, D. A.; Georgiadis, N. J. (1999): Implementation and validation of the Chien k-ε turbulence model in the Wind Navier-Stokes code, *NASA Technical Memorandum 209080.*